Acta Materialia 203 (2021) 116498

Contents lists available at ScienceDirect

Acta Materialia

journal homepage: www.elsevier.com/locate/actamat

Tracer diffusion in the σ phase of the CoCrFeMnNi system

Jingfeng Zhang[a], G. Mohan Muralikrishna[a,b], Alex Asabre[c], Yordan Kalchev[c], Julian Müller[d], Benjamin Butz[d], Sven Hilke[a], Harald Rösner[a], Guillaume Laplanche[c], Sergiy V. Divinski[a,e,*], Gerhard Wilde[a]

[a] Institute of Materials Physics, University of Münster, Germany
[b] Department of Metallurgical & Materials Engineering, IITM, Chennai, India
[c] Institut für Werkstoffe, Ruhr-Universität Bochum, Germany
[d] Micro- and Nanoanalytics Group, University of Siegen, Germany
[e] Samara National Research University, Moskovskoye Shosse 34, Samara 443086, Russia

ARTICLE INFO

Article history:
Received 21 August 2020
Revised 5 November 2020
Accepted 13 November 2020
Available online 21 November 2020

Keywords:
diffusion
high-entropy alloy
CrMnFeCoNi
sigma phase
TCP phase

ABSTRACT

A single Cr-rich σ-phase alloy with a composition of $Co_{17}Cr_{46}Fe_{16.3}Mn_{15.2}Ni_{5.5}$ (at.%) and a tetragonal lattice structure was produced. The tracer diffusion coefficients of Ni and Fe were measured by secondary ion mass spectroscopy using the highly enriched ^{64}Ni and ^{58}Fe natural isotopes. On the homologous temperature scale, Ni and Fe diffuse in the σ phase faster as compared to the corresponding diffusion rates in the equiatomic and face-centered cubic CoCrFeMnNi alloy. In contrast, on the absolute temperature scale, these elements diffuse roughly at the same rates in both materials. Factors influencing element diffusion and phase stability of the σ phase compared to the equiatomic alloy are discussed.

Introduction

The concept of high-entropy alloys has been introduced by Yeh *et.al.* in 2004 [1] and is now the focus of intensive research. Due to the mixing of multiple principal elements forming simple (solid solution) crystal structures, HEAs are expected to exhibit superior physical and mechanical properties [1]. Four core effects were believed to be inherent to HEAs: the high-entropy effect, 'sluggish' diffusion, cocktail effect, and severe lattice distortion [1,2].

Among all the reported HEAs, the CoCrFeMnNi alloy is widely investigated and is also known as "Cantor" alloy [3]. It has been reported to have a single-phase face-centered cubic (FCC) structure at elevated temperatures and reveal attractive properties like high strength, improved corrosion resistance, and very good thermal stability [4-8]. However, recent reports showed the formation of a Cr-rich σ phase in nearly equiatomic CoCrFeMnNi alloys when they are long-term annealed in the temperature range of 600-850°C [9-14]. For example, Otto *et. al.* have studied the formation of σ phase in coarse-grained materials and observed micrometer-large σ-phase particles after prolonged annealing treatments of 500 days [9]. In contrast, σ-phase precipitation was found to occur at much faster rates (in less than one hour) in the same alloy with a nanocrystalline microstructure produced by severe plastic deformation [15], indicating that grain boundary diffusion can significantly enhance the precipitation kinetics of the σ phase [16].

The σ phase is a topologically close-packed (TCP) complex phase with a tetragonal structure (space group $P4_2/mnm$), which is often observed in austenitic stainless steels and superalloys [17-19]. There are two formula units and 30 atoms per unit cell. The composition ranges from AB_7 to A_7B, where A is a transition element from group IIIA to VIA and B is an element from group VIIA or VIIIA. Traditionally, binary σ phases in austenitic steels and superalloys were investigated [20-23]. The σ phase was observed to precipitate at grain boundaries and grow along the boundary or into the adjacent matrix. For example, in steels, the main constituent element of the σ phase, like Cr, diffuses from the matrix and precipitate at grain boundaries in the form of Cr-rich carbides. Subsequent grain boundary diffusion facilitates the formation of the σ phase in austenitic stainless steels [20,24,25]. Diffusion in the σ phase is considered to be much slower and it is typically neglected in the literature [24,26]. Sometimes, carbide particles are still retained within the σ phase which was attributed to a low diffusivity in the σ phase [24].

Kucera *et al.* reported the diffusion coefficients of ^{48}V in the σ phase corresponding to the Fe-49.3 at.%V alloy [26]. To the best of our knowledge, there are no other reports on diffusion in the σ

* Corresponding author.
E-mail address: divin@uni-muenster.de (S.V. Divinski).

https://doi.org/10.1016/j.actamat.2020.116498

phase composed of elements of the Cantor (CoCrFeMnNi) system. The diffusion coefficients of V in the σ phase were found to be lower than those extrapolated from the body-centered cubic (BCC) solid solution and approached the factor of 33 at the phase transformation temperature of 1473 K [26]. This agrees generally with the fact that the atomic packing factor of the σ phase is larger than that of the BCC phase with the same composition.

Laplanche *et al.* studied the σ-phase precipitation kinetics in the off-equiatomic $Co_{20}Cr_{26}Fe_{20}Mn_{20}Ni_{14}$ HEA and determined a TTT diagram [11]. However, diffusion in a multicomponent σ phase was experimentally not investigated. Tracer diffusion of all constituting elements in equiatomic CoCrFeMnNi is well documented now [27-30]. These results and those for the FCC $Ni_x(CoCrFeMn)_{100-x}$ alloys ($20 \leq x \leq 100$) [31,32] substantiated that the concept of 'sluggish' diffusion cannot be used as a blanket statement, and enhancement or retardation of diffusion rates can be seen on the homologous temperature scale in dependence on the particular element or alloy. Here, the homologous temperature is defined as T/T_m, where T_m is the melting point of the corresponding compound. Thus, direct determination of the element diffusion rates in the σ phase is imperative for adequate forecasting of long-term phase stability of high-entropy alloys in the CoCrFeMnNi system. Furthermore, it is important to know the diffusion rates in the σ phase with respect to those in the Cantor alloy, since diffusion in the σ phase is traditionally thought to be slow [2,28,29,31,33-36]. For all these reasons, the present study is focused on experimental measurements of Ni and Fe tracer diffusion in the $Co_{17}Cr_{46}Fe_{16.3}Mn_{15.2}Ni_{5.5}$ σ-phase alloy relevant to the Cantor system.

Experimental details

Manufacturing of the alloy

Small buttons of σ phase with the nominal composition $Co_{17}Cr_{46}Fe_{16.3}Mn_{15.2}Ni_{5.5}$ (in at.%) and a targeted weight of 70 g were prepared from a mixture of pure metals in an arc-melter under Ti-gettered Ar-atmosphere. High-purity (better than 99.89 wt.%) metals were used. Before melting, the Mn and Co flakes were cleaned with distilled water and subsequently etched in aqueous solutions of either hydrochloric acid (18.5 vol.% HCl) for Co or nitric acid (> 5 vol.% HNO_3) for Mn. The detailed etching procedure is given in a previous report [37]. While noticing elemental losses of Mn due to evaporation, 0.2 wt.% extra Mn was added to compensate for these Mn losses. The arc-melted buttons were subsequently aged at 1100°C for three days to stabilize the σ phase and furnace cooled to impede crack initiation by minimizing thermal stresses during cooling. The annealed buttons were electrical-discharge machined (EDM) into 4-mm thick slices perpendicular to the largest section of the buttons. These slices revealed a high density of cracks and it is still unclear, whether the cracks were formed within the buttons during EDM, cooling after melting, or annealing. Finally, prior to microstructural investigations, the slices were ground to a grid size of 7 μm with SiC abrasive papers and electropolished for 8 s at 40 V using a "Struers" A2 electrolyte comprising 70 vol.% ethanol, 12 vol.% distilled water, 8 vol.% (70-72%) perchloric acid, and 10 vol.% diethylenglycolmonobuthylethen.

Alloy characterization

A small piece of the σ-phase alloy was crushed into powder, annealed in an evacuated quartz tube filled with purified (5N pure) Ar at 673 K for 3 hours to relieve internal stresses, and analyzed by X-ray diffraction (XRD, Siemens D5000).

Differential thermal analysis (DTA) was used to determine phase transformation temperatures. A piece of the sample weighing ~200 mg was inserted in an alumina crucible. DTA was performed at 30 K/min heating rate under purified Ar flow and two DTA cycles were performed without removing the sample from the apparatus. The two signals were found to be similar within the experimental accuracy.

Backscatter electron (BSE) micrographs with a resolution of 2048 × 1887 pixels were obtained using a scanning electron microscope (SEM) FEI Quanta 650 FEG at a working distance of 10 mm with an applied accelerating voltage of 20 kV. Besides, the texture and grain size of the as-cast and annealed buttons were subsequently investigated by electron backscatter diffraction (EBSD) using a high-performance FE-SEM JEOL JSM-7200F operating at an accelerating voltage of 30 kV, equipped with a "Symmetry" CCD camera and the "AZtec" analytical software from "Oxford Instruments". The EBSD experiments were carried out using a working distance of 15 mm and a 1-μm step size. Energy dispersive spectroscopy (EDS) was also used to verify the chemical homogeneity of the σ-phase alloy.

High-resolution transmission electron microscopy (HR-TEM) was performed with a Thermo Fisher Scientific Themis 300 G3 transmission electron microscope (TEM) to investigate the crystalline structure of the σ phase. The microscope was equipped with a high brightness field emission gun (X-FEG), a monochromator, an image Cs-corrector, a quadrupole energy-dispersive X-ray (EDX) system, a high-angle annular dark-field (HAADF) detector (Fischione Model 3000), a fast CMOS camera (Ceta, 4k x 4k) and a high-resolution electron energy loss (EEL) spectrometer (Quantum 965 Gatan Imaging Filter). The microscope was operated at an acceleration voltage of 300 kV with an extraction voltage of 3.45 kV for the X-FEG. Moreover, high-angle annular dark-field scanning transmission electron microscopy (HAADF-STEM) imaging was used to confirm that the observed features in HR-TEM micrographs were not artificial due to plural scattering.

Tracer diffusion measurements

Samples were cut into discs with a diameter of 8 mm and a thickness of 1 mm by spark erosion. All discs were then pre-annealed to reduce stresses and achieve equilibrium defect concentrations at the intended diffusion temperature. Annealing was performed in an evacuated quartz tube filled with purified (5N pure) Ar.

Inactive highly-enriched (> 98%) ^{64}Ni and ^{58}Fe isotopes were utilized for the current diffusion measurements. A thin, 30 to 40 nm thick, layer of either ^{64}Ni or ^{58}Fe was typically deposited on mirror-like polished samples using a physical vapor deposition (PVD) device in a vacuum better than 10^{-5} mbar. Diffusion annealing treatments were then carried out in sealed quartz tubes under purified (5N pure) Ar atmosphere. Annealing times and temperatures used to get appropriate diffusion depths are given in Table 1. In addition, two sets of deposition were conducted to verify the feasibility and accuracy of the experiments. Only ^{64}Ni tracer and mixed tracers of ^{64}Ni and ^{58}Fe were deposited for the first and second sets of samples, respectively. The annealing temperatures and times were chosen following a trial-and-error procedure using the previously determined tracer diffusion coefficients of Ni and Fe in CoCrFeMnNi HEA [29,30]. The intended diffusion lengths, $\sqrt{4Dt}$, were tried to keep between 500 and 3000 nm to produce reliable data.

The composition profiles for ^{64}Ni and ^{58}Fe diffusion were probed by Time-of-Flight Secondary Ion Mass Spectrometry (ToF-SIMS, IONTOF„TOF.SIMS^5-300"). SIMS is a highly sensitive technique, which provides ppm level sensitive information on the atomic and molecular composition of the uppermost 1 - 3 monolayers. The final depth of the crater formed during the ToF-SIMS measurement was determined by means of confocal interferom-

Table 1
Annealing time, temperature, and the determined diffusion coefficients for Ni and Fe in the σ phase. The typical experimental uncertainties are estimated to be less than about 10%.

Tracers	Temperature (K)	Annealing time (10^3 s)	Diffusion Coefficients (m^2/s)
^{64}Ni	928	2160	6.94×10^{-21}
^{64}Ni	943	2397.6	1.13×10^{-20}
^{64}Ni	973	608.4	5.68×10^{-20}
^{64}Ni	987	604.8	6.48×10^{-20}
^{64}Ni	1023	108	2.62×10^{-19}
^{64}Ni	1069	58.8	1.01×10^{-18}
^{64}Ni	1128	31.3	6.88×10^{-18}
^{64}Ni	1173	14.4	1.51×10^{-17}
^{64}Ni	1173	10.8	2.01×10^{-17}
^{58}Fe	943	2397.6	7.47×10^{-21}
^{58}Fe	987	604.8	7.44×10^{-20}
^{58}Fe	1069	58.8	8.82×10^{-19}
^{58}Fe	1173	10.8	2.17×10^{-17}

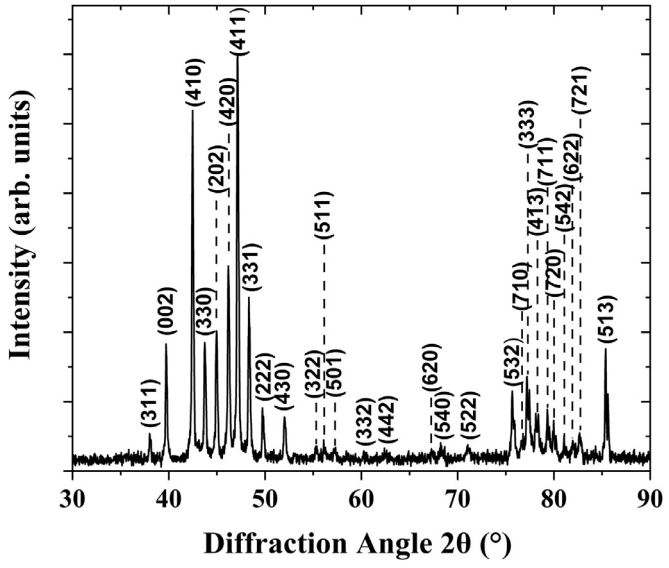

Fig. 1. X-ray diffraction pattern of the $Co_{17}Cr_{46}Fe_{16.3}Mn_{15.2}Ni_{5.5}$ alloy. Peaks corresponding to the crystallographic planes of the σ phase are indicated.

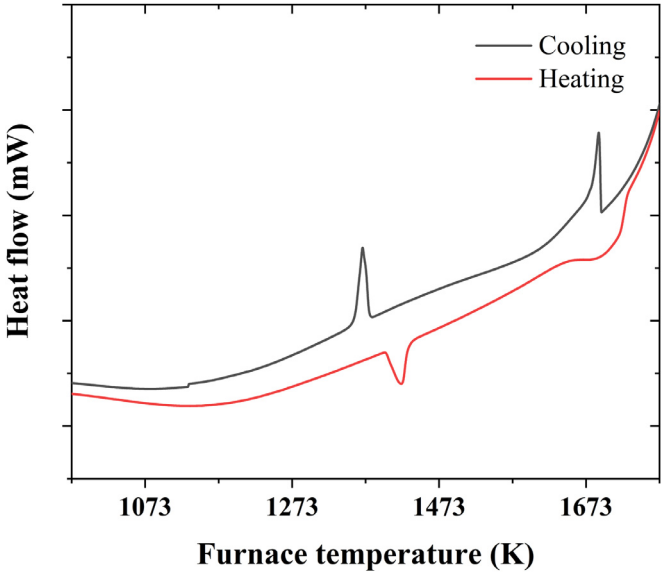

Fig. 2. DTA thermogram of the σ phase $Co_{17}Cr_{46}Fe_{16.3}Mn_{15.2}Ni_{5.5}$ as measured with a constant heating rate of 30 K/min.

etry in order to establish a depth scale to the ToF-SIMS profile. ToF-SIMS in the double beam mode was used for data acquisition. A sputter beam of O_2^+ (2 keV) was applied to erode the sample while the second ion beam of Bi^+ (25 keV) was used for the chemical characterization of the resulting crater bottom. The SIMS measurements were conducted in a 50 × 50 μm^2 area, which was chosen in the center of an area larger than 200 × 200 μm^2 without any defects like cracks or second phases. Such crack-free areas were carefully selected by optical and electron microscopy. Thus the measured diffusion profiles were not affected by the presence of these defects. Moreover, special precautions were taken to select areas without grain boundaries to provide reliable volume diffusion rates.

Results

Microstructure and chemical homogeneity of the aged σ phase

The XRD pattern presented in Fig. 1 reveals only diffraction peaks belonging to the tetragonal crystallographic structure of a σ intermetallic compound with the lattice parameters a and c determined as 0.8783 and 0.4543 nm, respectively. As phases with low volume fractions cannot be detected by XRD, further EBSD and TEM analyses were conducted.

The DTA heat flow is shown as a function of temperature in Fig. 2 where the red and black curves were recorded upon heating and cooling, respectively. Two endothermic peaks are observed at ~1423 K and ~1682 K upon heating in Fig. 2. Based on a comparison of the DTA curves with the phase diagrams of binary σ intermetallics (FeCr and FeV), it is likely that these endothermic peaks correspond to a σ-BCC transformation (1423 K) and melting (1682 K) but further works are still needed to confirm this.

A multiscale characterization of the as-cast and aged σ phase is sketched in Fig. 3. A schematic overview of the aged button shows a major σ phase (gray color) with the presence of a band of secondary phase particles (highlighted with red color) located close to the equatorial plane of the button as shown in Fig. 3a. The area marked with a dark blue rectangle in Fig. 3a is magnified in Fig. 3b. The magnified view (Fig. 3b) is a BSE image revealing the presence of several cracks, the σ matrix in gray, and second phase particles with a darker contrast. Most of these latter particles contain annealing twins (see blue arrows in Fig. 3c), indicating the possible presence of an FCC crystal structure. Further work is still required to identify the nature of these second-phase particles, which surface area fraction averaged over the whole button was estimated to be ~1% using an image analysis software "ImageJ". In other words, the button consists of ~99% of σ phase, which will allow us to in-

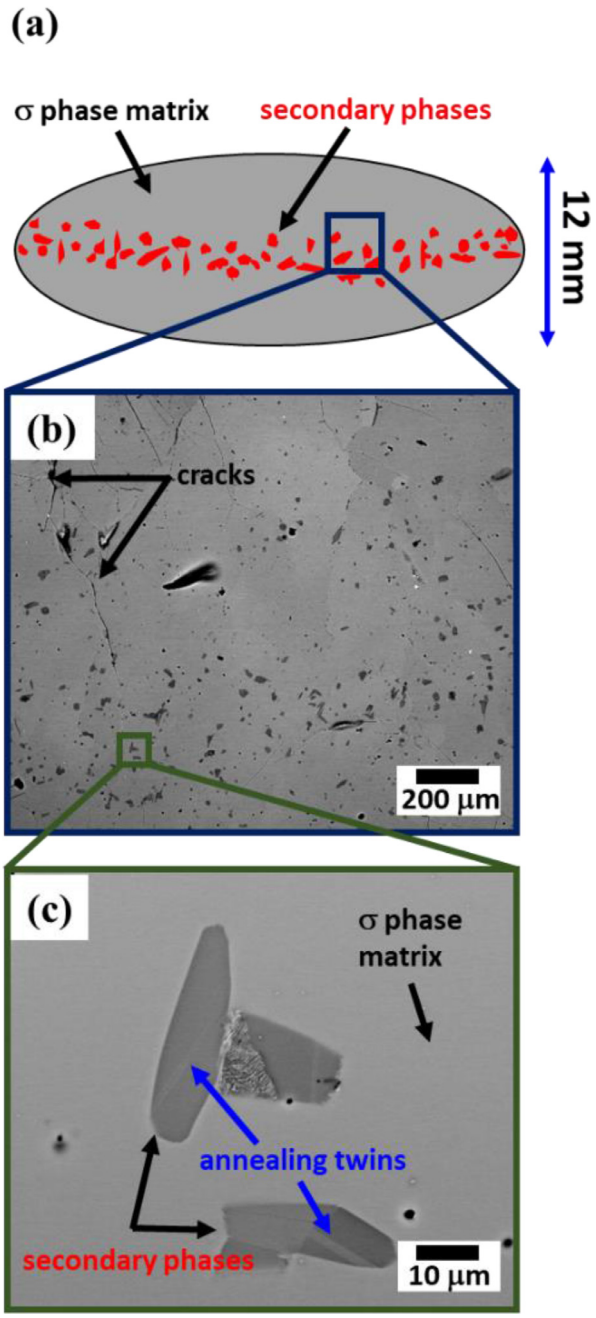

Fig. 3. Microstructural investigation of a σ-phase $Co_{17}Cr_{46}Fe_{16.3}Mn_{15.2}Ni_{5.5}$ (in at.%) alloy. (a) Scheme of the cross-section of an arc-melted and annealed button which mainly consists of σ phase (grey) with a band of second-phase particles (red) located in the equatorial plane. (b) Low-magnification BSE image of the microstructure showing cracks, the σ matrix, and a band of secondary phases in the lower half of the picture. (c) High-magnification BSE image of the secondary phases. One of the secondary phases contains annealing twins marked with blue arrows while the phase in the middle of the image exhibits a lamellar structure. The dark particles next to the scale bar are oxides containing Mn and Cr.

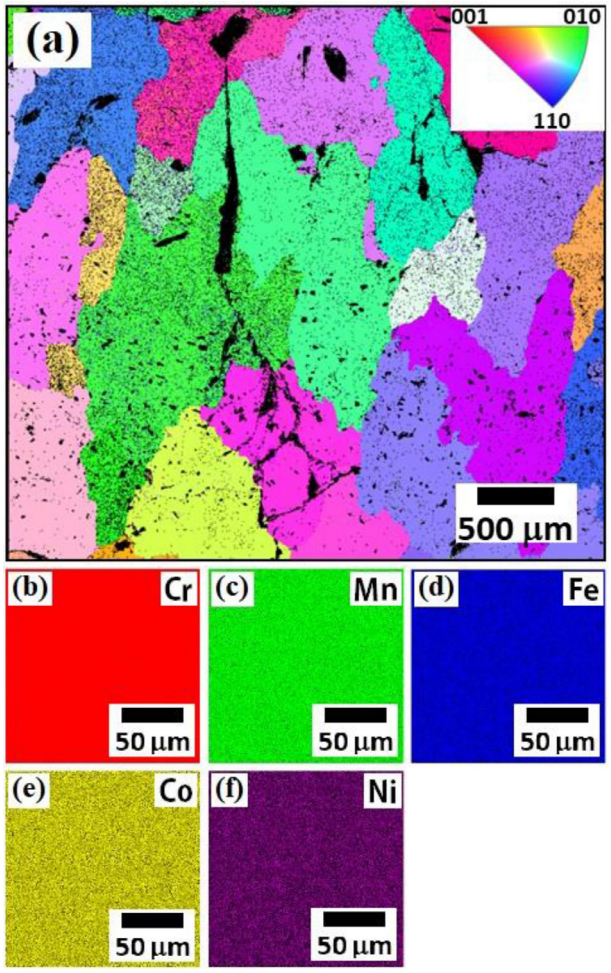

Fig. 4. (a) EBSD grain orientation map (3.4 mm × 3.1 mm) of a σ phase $Co_{17}Cr_{46}Fe_{16.3}Mn_{15.2}Ni_{5.5}$. The grain colors correspond to the orientations of the crystallographic planes with respect to the upward direction (stereographic triangle is shown as insert). Representative elemental EDX maps show uniform distributions of Cr (b), Mn (c), Fe (d), Co (e), and Ni (f) atoms. Note that the EBSD and EDX analyses were performed on two distinct specimens.

vestigate its intrinsic properties. Note that care was taken to perform the SIMS measurements in regions that were devoided of second phase particles.

Since the grains of the σ phase can hardly be distinguished in Fig. 3b, EBSD was used to obtain the grain orientation map as shown in Fig. 4a. A coarse-grained microstructure (d > 500 µm) exhibiting no particular texture can be observed. As the mean grain size is much larger than the region analysed by SIMS measurements (50 × 50 μm^2), the diffusion data reported in the following are therefore representative of volume diffusion in single crystals. The EDS analysis shown in Figs. 4b-f confirms the homogeneous elemental distribution in the diffusion zone.

To explore further the microstructure at the atomic scale, TEM investigations were carried out. Figs. 5a and 5b show an HR-TEM micrograph projected along the [011] direction and the corresponding Fourier transform (power spectrum), respectively. The observed atomic structure matches with that of rutile ($P4_2/mnm$, space group no. 136 tetragonal primitive), see simulated red-framed inset in Fig. 5a, with 30 atoms distributed over five inequivalent site positions in the unit cell (Fig. 5d). For the particular simulation, an absence of a site preference of elements was assumed. Note that the complex crystallographic structure of σ phases was discovered long ago [17-19] and a certain site preference for constituting atoms was predicted, e.g., for Cr-based binary σ phases [38-40].

From the electron diffraction pattern (Fig. 5b) the following values were determined for the lattice parameters along the *a*- and *c*-axes: $a = 0.872$ nm and $c = 0.45$ nm. These values are in good agreement with the lattice parameters obtained by XRD. Moreover, it is worth noting that the features appearing horizontally in the HR-TEM micrograph (Fig. 5a) are not related to twins or double diffraction since multi-slice TEM imaging simulations using JEMS

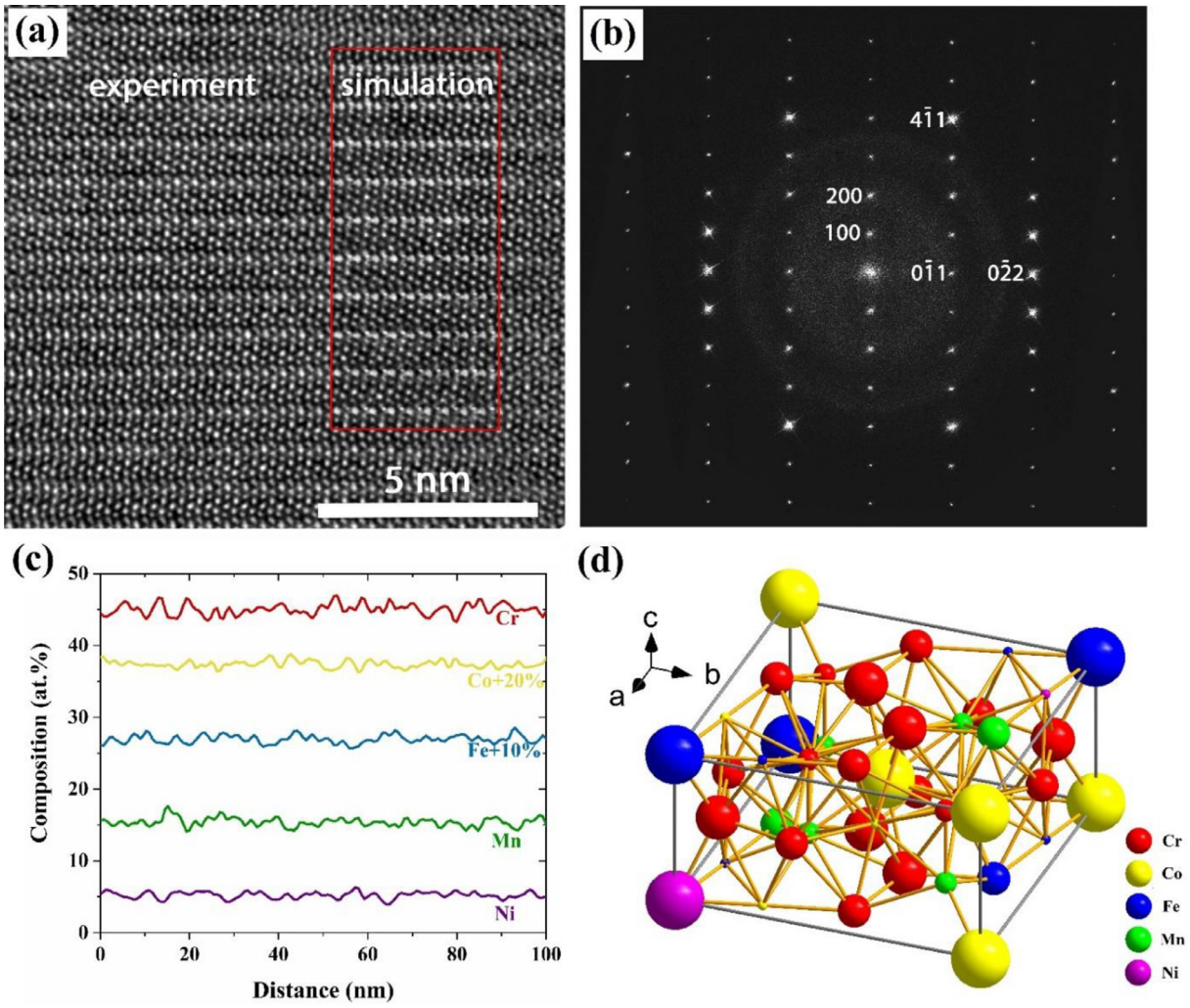

Fig. 5. (a) HR-TEM micrograph showing the structure of the σ phase projected along the [011] direction, together with the TEM imaging simulation. (b) corresponding power spectrum showing the [011] zone axis. (c) EDX profiles of a line scan revealing a chemically homogeneous σ phase without any segregation or decomposition. (d) A possible element distribution between sites of a unit cell of the σ phase alloy with the average composition (in at.%) $Co_{17}Cr_{46}Fe_{16.3}Mn_{15.2}Ni_{5.5}$ with given 30 atoms distributed over five crystallographically inequivalent sites (the atom types were randomly chosen mimicking the given alloy composition). The different sizes and colors of spheres in the figure represent five nonequivalent sites and five elements, respectively. Note that a larger supercell has to be used to account for the correct alloy composition.

[41] excluded this. The contrast indicates a large-unit cell lattice structure with a layer-type packing of atoms. The corresponding chemical analysis (EDX) shown in Fig. 5c revealed a homogeneous composition of the σ phase at the nanoscale without evidence for segregation or decomposition.

Diffusion measurements

As an example, the concentration profiles of ^{64}Ni and ^{58}Fe in the sample annealed at 1173 K for 4 h are shown in Fig. 6. The instantaneous source (Gaussian) solution of the bulk diffusion problem is found to be appropriate and the concentration profiles were fitted accordingly [42],

$$C(x,t) = \frac{M}{\sqrt{\pi Dt}} \exp\left(-\frac{x^2}{4Dt}\right) + C_0 \quad (1)$$

Here $C(x,t)$ is the concentration at the depth x from the surface after the time t, D is the diffusion coefficient, M is the initial tracer amount, and C_0 is the background value corresponding to a natural abundance of the ^{64}Ni and ^{58}Fe isotopes (about 0.9% and 0.3% in pure metals, respectively).

Contributions of grain boundary diffusion were not observed. A relative uncertainty of the determined diffusion coefficients was less than 10%. The determined volume diffusion data are listed in Table 1. By analyzing the whole dataset, we conclude that the anisotropy of both Ni and Fe diffusion in the tetragonal lattice of the σ phase is almost negligible, i.e., the ratio of the diffusion coefficients along the two basic directions is about unity, since the diffusion rates measured on different samples for grains with different crystallographic orientations at different temperatures lie on a common Arrhenius-type line, see Fig. 7a. Note that due to the large grain size, it was possible to locate the areas of SIMS profiling within one particular grain.

The temperature dependencies of the diffusion coefficients in Fig. 7a are found to follow the Arrhenius behavior,

$$D = D_0 \exp\left(-\frac{Q}{RT}\right) \quad (2)$$

where D_0 is the pre-exponential factor, Q is the activation energy, and RT has its usual meaning. The diffusion rates of Fe and Ni atoms are found to be quite similar, as it was observed in the CoCrFeMnNi HEA and the CrFeCoNi MEA [28,29,31] and in pure Ni [43-46].

The activation energies, Q, are determined to be (290±6) kJ/mol and (311±15) kJ/mol, and the pre-exponential factors are

Table 2
Activation energy Q and pre-exponential factor D_0 of all the alloying systems analyzed in the present work.

Tracers	Alloys	Q (kJ/mol)	D_0 (m^2/s)	References
Ni	$Co_{17}Cr_{46}Fe_{16.3}Mn_{15.2}Ni_{5.5}$	290±6	$1.58^{-0.79}_{+1.61} \times 10^{-4}$	Present work
Fe	$Co_{17}Cr_{46}Fe_{16.3}Mn_{15.2}Ni_{5.5}$	311±15	$1.54^{-1.26}_{+7.16} \times 10^{-3}$	Present work
Ni	CoCrFeMnNi HEA	304	6.2×10^{-4}	[30]
Fe	CoCrFeMnNi HEA	309	1.3×10^{-3}	[29]
V	FeV σ phase alloy	252	1.1×10^{-5}	[26]
V	FeV α phase alloy	293	4.5×10^{-3}	[26]

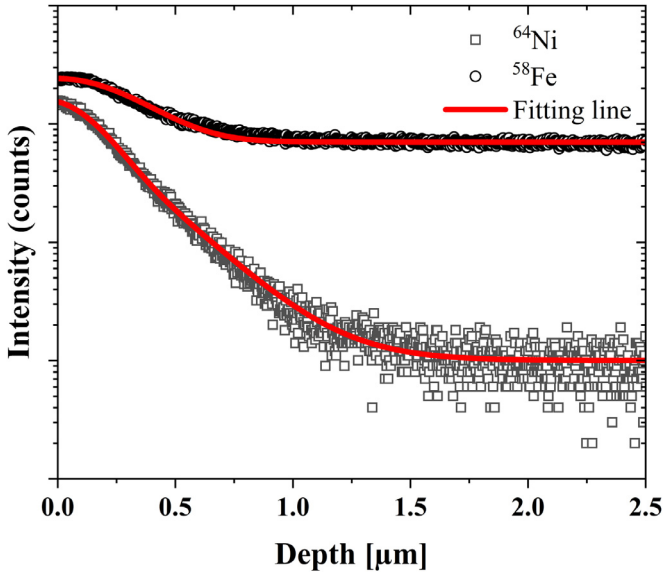

Fig. 6. Composition profiles of ^{58}Fe and ^{64}Ni annealed at 1173 K for 4 h obtained by ToF-SIMS.

$(1.58^{-0.8}_{+1.6}) \times 10^{-4}$ m^2/s and $(1.54^{-1.3}_{+7.2}) \times 10^{-3}$ m^2/s for Ni and Fe, respectively.

Discussion

In Fig. 7, the determined tracer diffusion coefficients in the σ phase are compared with those in several relevant systems. First, tracer diffusion of Fe and Ni in the coarse-grained polycrystalline [29,30] equiatomic CoCrFeMnNi alloy is considered owing to the same alloying elements. Finally, tracer diffusivities of vanadium in the binary Fe-V σ phase [26] are shown since these are the only σ-phase diffusion data available in the literature.

The diffusion rates scale typically with the corresponding melting points of the materials, T_m, for a detailed discussion see, e.g., [47]. As a result, both the inverse absolute temperature scale, $1/T$, and the inverse homologous temperature scale, T_m/T, are used here to gain a comprehensive understanding.

If compared on the inverse absolute temperature scale, Fig. 7a, the tracer diffusion rates of Fe and Ni in the σ phase of the CoCrFeMnNi system are quite similar to those in the equiatomic CoCrFeMnNi alloy in the whole temperature range. Both the activation energies and the pre-exponential factors for these two systems are similar, as shown in Table 2. If the diffusion rates are compared using the inverse homologous temperature scale, Fig. 7b, accelerated diffusion in the σ phase with respect to the equiatomic CoCrFeMnNi alloy is obvious. Such high diffusion rates in the σ phase of the CoCrFeMnNi system were not expected as discussed below.

Diffusion in the σ phase

The lattice structure of a binary σ phase is already very complex due to a high number of atoms (30) per unit cell having five distinct sublattices with high coordination numbers (12–15), each showing a certain chemical preference [17,18]; altogether this results in a huge number of possible atomic configurations. The five-component $Co_{17}Cr_{46}Fe_{16.3}Mn_{15.2}Ni_{5.5}$ σ phase features inevitably an even more complicated structure. The general formula of the σ phase can be defined as $A_2^{12}B_4^{15}C_8^{14}D_8^{12}E_8^{14}$, where the bottom and top indices denote the site multiplicities and the coordination numbers for each sublattice, respectively [48]. The site occupation in the σ phase is influenced by the composition and annealing conditions, and Cr prefers the high-coordination-number sites (B, C, and E) in binary phases [48,49]. One may expect similar trends in the present multi-component σ phase, too. Figure 5d shows the unit cell of a possible atomic structure of the quinary σ phase. The different atom sizes and colors represent the five nonequivalent sites (sublattices) and the five elements, respectively.

Deeper understanding could be obtained through atomistic calculations that address the underlying diffusion mechanisms. However, ab initio calculations for the five-component CoCrFeMnNi σ phase have to face the difficulty of a large unit cell and its chemical complexity to provide reliable data [50]. On the other hand, the mechanical and thermodynamic properties of the σ phase have to be carefully addressed before performing atomistic simulations using existing empirical potentials, as it was done for the CoCrFeMnNi HEAs, see e.g. [32,51]. In this paper, the present diffusion results are discussed using known experimental results.

In Fig. 7, the V diffusion rates in σ and disordered α (BCC) phases of the Fe-49.3 at.%V alloy [26] are compared with the present data, which offers valuable insights into the impact of the crystalline structure of the σ phase on self-diffusion. When extrapolated from high temperatures, V diffusion in the α phase is faster than that in the low-temperature σ phase and the diffusivity ratio, $D_V^{\alpha}/D_V^{\sigma}$, is about 33 at the α–σ transition temperature (1473K). This is not surprising because the σ phase is more closely packed than the α phase. However, the significantly lower activation energy of V diffusion in the σ phase (252 kJ/mol) with respect to that in the α phase (293 kJ/mol) is unexpected (Table 2). At first glance, the understanding of this fact is not straightforward because of two reasons:

- the Girifalco model [52] predicts an *increase* of the activation enthalpy with ordering; note that the σ phase with five sublattices and a certain site preference is more ordered with respect to an FCC solid solution with the same composition;
- one would expect *larger* activation energy of diffusion in a more closely packed structure, as it is the case, e.g., for Fe tracer diffusion in α- and γ-Fe [47].

Since at the same absolute temperatures $D_V^{\sigma} < D_V^{BCC}$ and the activation energy is smaller in the σ phase, the influence of the prefactors for diffusion has unambiguously to be discussed. Thus, the lower diffusion rates in the binary σ phase have to be attributed

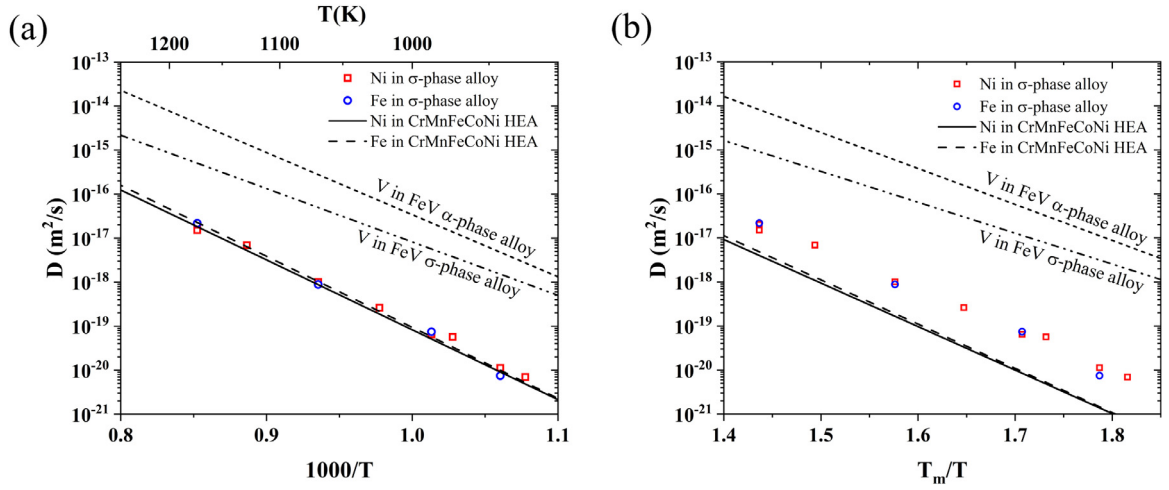

Fig. 7. Ni (squares, solid line) and Fe (circles, dashed line) diffusion in the $Co_{17}Cr_{46}Fe_{16.3}Mn_{15.2}Ni_{5.5}$ σ phase (symbols, this work) and in the equiatomic CoCrFeMnNi HEA [[29] (lines). For comparison, the diffusion rates of V in the Fe-V σ (dot-dashed line) and α (dashed line) phases [**26**] are shown. Since the α Fe-V phase is not stable in the given temperature range, the diffusion data were extrapolated from the Arrhenius equation given in Ref. [**26**]. The diffusion coefficients are plotted as functions of the inverse absolute (a) and inverse homologous (b) temperature scales, with T_m being the melting point of the corresponding material.

to a significantly lower pre-exponential factor, D_0, for V diffusion in the σ phase.

Diffusion in Cantor alloy and σ phase of the CoCrFeMnNi system

The difference of the diffusion rates in the σ phase ($Co_{17}Cr_{46}Fe_{16.3}Mn_{15.2}Ni_{5.5}$) and the fcc equiatomic CoCrFeMnNi alloy is affected by changes in composition, crystal structures, and partial site preference. In the case of vacancy-mediated self-diffusion, the activation energy is the sum of the vacancy formation and migration energies [42]. To the best of our knowledge, there are no investigations related to the vacancy formation or migration in the CoCrFeMnNi σ phase so far. The vacancy formation energies were recently determined for the equiatomic CoCrFeMnNi alloy by positron annihilation [53] and ab initio-informed calculations [54]. A relatively wide spectrum of migration barriers was predicted for vacancy–atom exchanges in the CoCrFeMnNi alloy [16]. The vacancy formation energies as a function of atomic environments, studied for CoCrNi and CoCrFeNi [55] and for CoCrFeMnNi [54], were found to increase generally with an increase of the number of Cr atoms and/or with a decrease of the number of Ni atoms in the corresponding first coordination shells.

According to the experimental facts established for binary Fe-V alloys, one may expect that the crystalline structure of the σ phase would lead to a *decrease* of the activation energy of diffusion with respect to the fcc lattice of the CoCrFeMnNi alloy with the same, i.e., Cr-enriched and Ni-depleted, composition. On the other hand, the Cr enrichment and Ni depletion in the fcc solid solution *increase* the diffusion activation enthalpy with respect to that in equiatomic CoCrFeMnNi alloy according to the DFT calculations [54]. Probably, these two factors almost compensate each other and the diffusion activation enthalpies are measured to be very similar in equiatomic fcc random solid solution and Cr-enriched (Ni-depleted) σ phase, Table 2.

In addition, the high-entropy effect, i.e., a broad distribution of local jump barriers for vacancy diffusion in the presence of multi-component environments, was thought to slow down the diffusion with respect to pure metals [1,2]. However, the recent studies related to tracer diffusion in the Cantor system suggested that high mixing entropy has a very limited impact on the diffusion compared with other influencing factors [29-31, 56]. In the present study, the mixing entropy of $Co_{17}Cr_{46}Fe_{16.3}Mn_{15.2}Ni_{5.5}$ σ phase is ~1.40R, if the partial site preference is neglected. The actual mixing entropy will be smaller, temperature-dependent, and definitely smaller than that of Cantor alloy (1.61R). Therefore, the configurational entropy should not be considered as one of the main reasons that influence the diffusion in the CoCrFeMnNi σ phase.

Diffusion in CoCrFeMnNi alloying system

The present measurements of tracer diffusion in the σ phase extend the existing datasets for the CoCrFeMnNi system, for which tracer diffusion in single-crystalline [56] and polycrystalline [29,30] equiatomic alloys has been investigated, as well as interdiffusion [2,28] and grain boundary diffusion [16,57]. Furthermore, tracer diffusion in off-equiatomic CoCrFeMnNi alloys was examined, too [31,32]. These kinetic data are required for both the design of CoCrFeMnNi HEAs and the understanding of many important phenomena, such as phase stability and precipitation kinetics of the σ phase.

One may attribute the appearance of the Cr-rich σ phase in CoCrFeMnNi alloys to the rapid diffusion of Cr element at intermediate temperatures when diffusion data is not available [58]. But later studies showed that the diffusion of Cr in the CoCrFeMnNi alloy is not the fastest compared with other alloying elements in both bulk and grain boundary diffusion [16,29,30,57]. The measured activation energy of Cr grain boundary diffusion in CoCrFeMnNi (180 kJ/mol) [16] correlates with the apparent activation energy of (195±15) kJ/mol for σ phase formation in the CoCrFeMnNi HEA system [11]. This fact suggests that nucleation and growth of the σ phase could be significantly promoted by fast diffusion along grain boundaries.

Although the thermodynamic instability of the single-phase FCC CoCrFeMnNi alloy at low temperatures has been proven and the precipitation of the σ phase is undesirable under most circumstances, some studies are aiming at utilizing the σ phase as strengthening particles in several different HEA systems [59-63]. When considering to either keep or remove the σ precipitates, the rate-controlling mechanism should be governed by the slowest diffusion process which is more likely to be bulk diffusion in FCC phase for precipitation and diffusion in σ phase for dissolution. In addition, diffusion along FCC/σ phase interfaces, which was first investigated in Ref. [64], is also of vital importance and requires further research using radiotracers. Even though the growth kinetics of micrometer-sized σ precipitates is controlled by diffusion in the FCC phase [64], the relatively high diffusion rates in the

σ phase may play a role on the nucleation and growth kinetics of σ nanoprecipitates.

Conclusions

A single-phase $Co_{17}Cr_{46}Fe_{16.3}Mn_{15.2}Ni_{5.5}$ (in at.%) alloy (σ phase) with a tetragonal crystallographic structure was produced and characterized using XRD, DTA, BSE, EDS, EBSD, and TEM. Volume diffusion of Ni and Fe were measured for the first time in this alloy utilizing SIMS. The main results can be summarized as follows:

- The measured tracer diffusion coefficients of Ni and Fe are in the range of 10^{-21} to 10^{-17} m^2/s between 928 and 1173 K. The difference between the diffusion coefficients of these two tracers is quite small.
- An unexpected accelerated bulk diffusion has been found in the compositionally complex σ phase compared with the equiatomic CoCrFeMnNi alloy when the homologous temperature is used for comparison. In contrast, using the absolute temperature scale, diffusion in both the quinary σ phase and the equiatomic CoCrFeMnNi HEA occurs roughly at the same rate in the investigated temperature range.
- The unexpected relatively fast diffusion of Ni and Fe in the $Co_{17}Cr_{46}Fe_{16.3}Mn_{15.2}Ni_{5.5}$ σ phase correlates with literature experimental data on V diffusion in binary σ phase and α disordered solid solution Fe-V alloys.

Declaration of Competing Interest

The authors declare that they have no known competing financial interests or personal relationships that could have appeared to influence the work reported in this paper.

Acknowledgments

Jingfeng Zhang is grateful to the China Scholarship Council (CSC) for financial support. G. Mohan Muralikrishna is grateful to the German academic exchange service (DAAD) for awarding a fellowship to conduct tracer diffusion experiments at the University of Münster, Germany. Fi-nancial support by the German Research Foundation (DFG) via research grants DI 1419/13-2 and LA3607/3-2 in the framework of the priority program SPP 2006 – Compositionally Complex Al-loys - High Entropy Alloys are acknowledged. The DFG is further acknowledged for funding our TEM equipment via the Major Research Instrumentation Program under INST 211/719-1 FUGG. The center for interface dominated high performance materials (Zentrum für Grenzflächendomi-nierte Höchstleistungswerkstoffe, ZGH) is acknowledged for the use of the JEOL JSM-7200F SEM. Part of this work was performed at the Micro- and Nanoanalytics Facility (MNaF) of the University of Siegen.

References

[1] J.W. Yeh, S.K. Chen, S.J. Lin, J.Y. Gan, T.S. Chin, T.T. Shun, C.H. Tsau, S.Y. Chang, Nanostructured high-entropy alloys with multiple principal elements: novel alloy design concepts and outcomes, Advanced Engineering Materials 6 (5) (2004) 299–303.
[2] K.Y. Tsai, M.H. Tsai, J.W. Yeh, Sluggish diffusion in Co–Cr–Fe–Mn–Ni high-entropy alloys, Acta Materialia 61 (13) (2013) 4887–4897.
[3] B. Cantor, I.T.H. Chang, P. Knight, A.J.B. Vincent, Microstructural development in equiatomic multicomponent alloys, Materials Science & Engineering A 375-377 (1) (2004) 213–218.
[4] B. Gludovatz, A. Hohenwarter, D. Catoor, E.H. Chang, E.P. George, R.O. Ritchie, A fracture-resistant high-entropy alloy for cryogenic applications, Science 345 (6201) (2014) 1153.
[5] F. Zhang, C. Zhang, S.L. Chen, J. Zhu, W.S. Cao, U.R. Kattner, An understanding of high entropy alloys from phase diagram calculations, Calphad 45 (2014) 1–10.
[6] Y. Zhang, T.T. Zuo, Z. Tang, M.C. Gao, K.A. Dahmen, P.K. Liaw, Z.P. Lu, Microstructures and properties of high-entropy alloys, Prog. Mater Sci. 61 (8) (2014) 1–93.
[7] Z.J. Zhang, M.M. Mao, J. Wang, B. Gludovatz, Z. Zhang, S.X. Mao, E.P. George, Q. Yu, R.O. Ritchie, Nanoscale origins of the damage tolerance of the high-entropy alloy CrMnFeCoNi, Nature Communications 6 (2015) 10143.
[8] Y.K. Kim, Y.A. Joo, H.S. Kim, K.A. Lee, High temperature oxidation behavior of Cr-Mn-Fe-Co-Ni high entropy alloy, Intermetallics 98 (2018) 45–53.
[9] F. Otto, A. Dlouhý, K.G. Pradeep, M. Kuběnová, D. Raabe, G. Eggeler, E.P. George, Decomposition of the single-phase high-entropy alloy CrMnFeCoNi after prolonged anneals at intermediate temperatures, Acta Materialia 112 (2016) 40–52.
[10] E.J. Pickering, R. Muñoz-Moreno, H.J. Stone, N.G. Jones, Precipitation in the equiatomic high-entropy alloy CrMnFeCoNi, Scripta Materialia 113 (2016) 106–109.
[11] G. Laplanche, S. Berglund, C. Reinhart, A. Kostka, F. Fox, E.P. George, Phase stability and kinetics of σ-phase precipitation in CrMnFeCoNi high-entropy alloys, Acta Materialia 161 (2018) 338–351.
[12] K. Christofidou, E. Pickering, P. Orsatti, P. Mignanelli, T. Slater, H. Stone, N. Jones, On the influence of Mn on the phase stability of the CrMnxFeCoNi high entropy alloys, Intermetallics 92 (2018) 84–92.
[13] M. Bloomfield, K. Christofidou, N. Jones, Effect of Co on the phase stability of CrMnFeCoxNi high entropy alloys following long-duration exposures at intermediate temperatures, Intermetallics 114 (2019) 106582.
[14] K. Christofidou, T. McAuliffe, P. Mignanelli, H. Stone, N. Jones, On the prediction and the formation of the sigma phase in CrMnCoFeNix high entropy alloys, Journal of Alloys and Compounds 770 (2019) 285–293.
[15] B. Schuh, F. Mendez-Martin, B. Völker, E.P. George, H. Clemens, R. Pippan, A. Hohenwarter, Mechanical properties, microstructure and thermal stability of a nanocrystalline CoCrFeMnNi high-entropy alloy after severe plastic deformation, Acta Materialia 96 (2015) 258–268.
[16] M. Glienke, M. Vaidya, K. Gururaj, L. Daum, B. Tas, L. Rogal, K. Pradeep, G. Wilde, S.V. Divinski, Grain boundary diffusion in CoCrFeMnNi high entropy alloy: kinetic hints towards a phase decomposition, Acta Materialia 195 (2020) 304–316.
[17] J.S. Kasper, The Crystal Structure of the Sigma-Phase in the Co-Cr System, Journal of Applied Physics 22 (3) (1951) 361–362.
[18] G. Bergman, D.P. Shoemaker, The determination of the crystal structure of the σ phase in the iron–chromium and iron–molybdenum systems, Acta Crystallographica 7 (12) (1954) 857–865.
[19] G.J. Dickins, A.M.B. Douglas, W.H. Taylor, The crystal structure of the Co–Cr σ phase, Acta Crystallographica 9 (3) (1956) 297–303.
[20] A. Perron, C. Toffolon-Masclet, X. Ledoux, F. Buy, T. Guilbert, S. Urvoy, S. Bosonnet, B. Marini, F. Cortial, G. Texier, C. Harder, V. Vignal, P. Petit, J. Farré, E. Suzon, Understanding sigma-phase precipitation in a stabilized austenitic stainless steel (316Nb) through complementary CALPHAD-based and experimental investigations, Acta Materialia 79 (2014) 16–29.
[21] F. Sun, J. Zhang, P. Liu, Q. Feng, X. Han, S. Mao, High resolution transmission electron microscopy studies of σ phase in Ni-based single crystal superalloys, Journal of Alloys and Compounds 536 (2012) 80–84.
[22] C.-C. Hsieh, W. Wu, Overview of Intermetallic Sigma Phase Precipitation in Stainless Steels, ISRN Metallurgy 2012 (2012) 1–16.
[23] M. Schwind, J. Källqvist, J.O. Nilsson, J. Ågren, H.O. Andrén, σ-Phase precipitation in stabilized austenitic stainless steels, Acta Materialia 48 (10) (2000) 2473–2481.
[24] T.H. Chen, J.R. Yang, Effects of solution treatment and continuous cooling on σ-phase precipitation in a 2205 duplex stainless steel, Materials Science & Engineering A 311 (1) (2001) 28–41.
[25] A. Malik, J. Odqvist, L. Höglund, S. Hertzman, J. Ågren, Phase-Field Modeling of Sigma-Phase Precipitation in 25Cr7Ni4Mo Duplex Stainless Steel, Metallurgical and Materials Transactions A 48 (10) (2017) 4914–4928.
[26] J. Kučera, K. Obrtlík, K. Cíha, Self-diffusion of V-48 in the FeV σ-phase and in an Fe-47 wt.% V solid solution, Czechoslovak Journal of Physics B 32 (8) (1982) 907–915.
[27] D. Gaertner, J. Kottke, Y. Chumlyakov, F. Hergemöller, G. Wilde, S.V. Divinski, Tracer diffusion in single crystalline CoCrFeNi and CoCrFeMnNi high-entropy alloys: Kinetic hints towards a low-temperature phase instability of the solid–solution? Scripta Materialia 187 (2020) 57–62.
[28] D. Gaertner, K. Abrahams, J. Kottke, V.A. Esin, I. Steinbach, G. Wilde, S.V. Divinski, Concentration-dependent atomic mobilities in FCC CoCrFeMnNi high--entropy alloys, Acta Materialia 166 (2019) 357–370.
[29] M. Vaidya, K.G. Pradeep, B.S. Murty, G. Wilde, S.V. Divinski, Bulk tracer diffusion in CoCrFeNi and CoCrFeMnNi high entropy alloys, Acta Materialia 146 (2018) 211–224.
[30] M. Vaidya, S. Trubel, B.S. Murty, G. Wilde, S.V. Divinski, Ni tracer diffusion in CoCrFeNi and CoCrFeMnNi high entropy alloys, Journal of Alloys and Compounds 688 (2016) 994–1001.
[31] J. Kottke, M. Laurent-Brocq, A. Fareed, D. Gaertner, L. Perrière, Ł. Rogal, S.V. Divinski, G. Wilde, Tracer diffusion in the Ni–CoCrFeMn system: Transition from a dilute solid solution to a high entropy alloy, Scripta Materialia 159 (2019) 94–98.
[32] J. Kottke, D. Utt, M. Laurent-Brocq, A. Fareed, D. Gaertner, L. Perrière, Ł. Rogal, A. Stukowski, K. Albe, S.V. Divinski, Experimental and theoretical study of tracer diffusion in a series of $(CoCrFeMn)_{100-x}Ni_x$ alloys, Acta Materialia 194 (2020) 236–348.
[33] S.V. Divinski, A.V. Pokoev, N. Esakkiraja, A. Paul, A Mystery of "Sluggish Diffusion" in High-Entropy Alloys: The Truth or a Myth? Diffusion Foundations 17 (2018) 69–104.

[34] W. Kucza, J. Dąbrowa, G. Cieślak, K. Berent, T. Kulik, M. Danielewski, Studies of "sluggish diffusion" effect in Co-Cr-Fe-Mn-Ni, Co-Cr-Fe-Ni and Co-Fe-Mn-Ni high entropy alloys; determination of tracer diffusivities by combinatorial approach, Journal of Alloys and Compounds 731 (2018) 920–928.
[35] T.R. Paul, I.V. Belova, G.E. Murch, Analysis of diffusion in high entropy alloys, Materials Chemistry and Physics 210 (2018) 301–308.
[36] R. Wang, W. Chen, J. Zhong, L. Zhang, Experimental and numerical studies on the sluggish diffusion in face centered cubic Co-Cr-Cu-Fe-Ni high-entropy alloys, Journal of Materials Science & Technology 34 (10) (2018) 1791–1798.
[37] M. Schneider, F. Werner, D. Langenkämper, C. Reinhart, G. Laplanche, Effect of Temperature and Texture on Hall–Petch Strengthening by Grain and Annealing Twin Boundaries in the MnFeNi Medium-Entropy Alloy, Metals 9 (1) (2019) 84.
[38] J. Havránková, J. Vřešťál, L. Wang, M. Šob, Ab initio analysis of energetics of σ-phase formation in Cr-based systems, Physical Review B 63 (17) (2001) 174104.
[39] J. Vřešťál, A. Kroupa, M. Šob, Application of ab initio electronic structure calculations for prediction of phase equilibria in superaustenitic steels, Computational materials science 38 (2) (2006) 298–302.
[40] M.H. Sluiter, K. Esfarjani, Y. Kawazoe, Site Occupation Reversal in the Fe−Cr σ Phase, Physical review letters 75 (17) (1995) 3142.
[41] https://www.jems-swiss.ch/Home/jemsWebSite/jems.html
[42] A. Paul, T. Laurila, V. Vuorinen, S.V. Divinski, Thermodynamics, diffusion and the Kirkendall effect in solids, Springer, 2014.
[43] H. Bakker, J. Backus, F. Waals, A curvature in the Arrhenius plot for the diffusion of iron in single crystals of nickel in the temperature range from 1200 to 1400 C, physica status solidi 45 (2) (1971) 633–638.
[44] M. Badia, A. Vignes, Interdiffusion and the Kirkendall Effect in Binary Alloys, MEM SCI REV MET 66 (12) (1969) 915–927.
[45] J. MacEwan, J. MacEwan, L. Yaffe, Diffusion of Ni63 in iron, cobalt, nickel, and two iron–nickel alloys, Canadian journal of chemistry 37 (10) (1959) 1629–1636.
[46] A. Vladimirov, V. Kajgorodov, S. Klotsman, I.S. Trakhtenberg, Volume diffusion of cobalt and tungsten in nickel, Fizika Metallov i Metallovedenie 46 (6) (1978) 1232–1239.
[47] H. Mehrer, Diffusion in solids: fundamentals, methods, materials, diffusion-controlled processes, Springer Science & Business Media2007.
[48] E. Kabliman, A.V. Ruban, P. Blaha, K. Schwarz, The Atomic Site Occupancies in the Fe-Cr σ-Phase, Solid State Phenomena 170 (2011) 13–16.
[49] E. Kabliman, P. Blaha, K. Schwarz, O.E. Peil, A.V. Ruban, B. Johansson, Configurational thermodynamics of the Fe-Crσ phase, Physical Review B 84 (18) (2011).
[50] Y. Ikeda, B. Grabowski, F. Körmann, Ab initio phase stabilities and mechanical properties of multicomponent alloys: A comprehensive review for high entropy alloys and compositionally complex alloys, Materials Characterization 147 (2019) 464–511.
[51] D. Farkas, Grain boundary structure in high-entropy alloys, Journal of Materials Science (2020) 1–11.
[52] L. Girifalco, Vacancy concentration and diffusion in order-disorder alloys, Journal of Physics and Chemistry of Solids 25 (3) (1964) 323–333.
[53] K. Sugita, N. Matsuoka, M. Mizuno, H. Araki, Vacancy formation enthalpy in CoCrFeMnNi high-entropy alloy, Scripta Materialia 176 (2020) 32–35.
[54] M. Mizuno, K. Sugita, H. Araki, Defect energetics for diffusion in CrMnFeCoNi high-entropy alloy from first-principles calculations, Computational Materials Science 170 (2019) 109163.
[55] S. Zhao, T. Egami, G.M. Stocks, Y. Zhang, Effect of d electrons on defect properties in equiatomic NiCoCr and NiCoFeCr concentrated solid solution alloys, Physical Review Materials 2 (1) (2018) 013602.
[56] D. Gaertner, J. Kottke, G. Wilde, S.V. Divinski, Y. Chumlyakov, Tracer diffusion in single crystalline CoCrFeNi and CoCrFeMnNi high entropy alloys, Journal of Materials Research 33 (19) (2018) 3184–3191.
[57] M. Vaidya, K. Pradeep, B. Murty, G. Wilde, S. Divinski, Radioactive isotopes reveal a non sluggish kinetics of grain boundary diffusion in high entropy alloys, Scientific reports 7 (1) (2017) 1–11.
[58] F. He, Z. Wang, Q. Wu, J. Li, J. Wang, C. Liu, Phase separation of metastable CoCrFeNi high entropy alloy at intermediate temperatures, Scripta Materialia 126 (2017) 15–19.
[59] W. Liu, Z. Lu, J. He, J. Luan, Z. Wang, B. Liu, Y. Liu, M. Chen, C. Liu, Ductile CoCrFeNiMox high entropy alloys strengthened by hard intermetallic phases, Acta Materialia 116 (2016) 332–342.
[60] K. Cho, Y. Fujioka, T. Nagase, H.Y. Yasuda, Grain refinement of non-equiatomic Cr-rich CoCrFeMnNi high-entropy alloys through combination of cold rolling and precipitation of σ phase, Materials Science and Engineering: A 735 (2018) 191–200.
[61] Y.H. Jo, W.-M. Choi, S.S. Sohn, H.S. Kim, B.-J. Lee, S. Lee, Role of brittle sigma phase in cryogenic-temperature-strength improvement of non-equi-atomic Fe-rich VCrMnFeCoNi high entropy alloys, Materials Science and Engineering: A 724 (2018) 403–410.
[62] M. Chen, L. Lan, X. Shi, H. Yang, M. Zhang, J. Qiao, The tribological properties of Al0. 6CoCrFeNi high-entropy alloy with the σ phase precipitation at elevated temperature, Journal of Alloys and Compounds 777 (2019) 180–189.
[63] Y. Jo, W. Choi, D. Kim, A. Zargaran, K. Lee, H. Sung, S.S. Sohn, H. Kim, B. Lee, S. Lee, Utilization of brittle σ phase for strengthening and strain hardening in ductile VCrFeNi high-entropy alloy, Materials Science and Engineering: A 743 (2019) 665–674.
[64] G. Laplanche, Growth kinetics of σ-phase precipitates and underlying diffusion processes in CrMnFeCoNi high-entropy alloys, Acta Materialia 199 (2020) 193–208.